

Programmable Self-Locking Origami Mechanical Metamaterials

Hongbin Fang,* Shih-Cheng A. Chu, Yutong Xia, and Kon-Well Wang

Developing mechanical metamaterials with programmable properties is an emerging topic receiving wide attention. While the programmability mainly originates from structural multistability in previously designed metamaterials, here it is shown that nonflat-foldable origami provides a new platform to achieve programmability via its intrinsic self-locking and reconfiguration capabilities. Working with the single-collinear degree-4 vertex origami tessellation, it is found that each unit cell can self-lock at a nonflat configuration and, therefore, possesses wide design space to program its foldability and relative density. Experiments and numerical analyses are combined to demonstrate that by switching the deformation modes of the constituent cell from prelocking folding to postlocking pressing, its stiffness experiences a sudden jump, implying a limiting-stopper effect. Such a stiffness jump is generalized to a multisegment piecewise stiffness profile in a multilayer model. Furthermore, it is revealed that via strategically switching the constituent cells' deformation modes through passive or active means, the n -layer metamaterial's stiffness is controllable among 2^n target stiffness values. Additionally, the piecewise stiffness can also trigger bistable responses dynamically under harmonic excitations, highlighting the metamaterial's rich dynamic performance. These unique characteristics of self-locking origami present new paths for creating programmable mechanical metamaterials with in situ controllable mechanical properties.

Mechanical metamaterial has become an important research area due to their unprecedented mechanical properties and performance that cannot be obtained in a bulk material. The unusual macroscale properties of metamaterials are primarily determined by purposefully designed small-scale architectures. For example, the pentamode metamaterials receive very large bulk modulus but very small shear modulus from specially designed conical-beam lattice structure;^[1,2] auxetic metamaterials with negative Poisson's ratio are achieved through various re-entrant structures, chiral structures, or rotating rigid structures;^[3–5] negative stiffness has also become a reality in metamaterials by exploiting the instability of the basic


structures.^[6–10] Recently, developing adaptive and programmable mechanical metamaterials and metastructures becomes another emerging area that receives wide attention.^[7,11–17] The main purpose of this direction is to control the structural mechanical behaviors and the associated functionalities through in-prior programming of the design or on-line tuning of the configuration.

In recent investigations, origami has been identified as an ideal platform to implement programmability in mechanical metamaterials. Origami is the ancient art of paper folding that transforms 2D flat sheets into complex 3D geometrical objects through delicate crease patterning and coordinated folding. Origami has received significant interests in diverse fields because of its excellent 3D shaping ability and simple tailoring of topology.^[18–23] Particularly, origami provides two powerful features to tailor mechanical properties: structural reconfigurability and structural multistability. On one hand, origami folding is an effective way to reconfigure the shape and alter the underlying topology. For example, the

well-studied Miura-ori tessellation is generalized to organize arbitrary smooth heterogeneously curved surfaces;^[24] and modular origami technique offers architected materials with extraordinary reconfigurability so that a wide range of qualitatively different characteristics can be obtained.^[25] On the other hand, bistability and multistability have been identified in certain origami patterns such that by switching among different stable states the structural mechanical properties can be reversibly reprogrammed.^[26–30] In addition to these, the scale independence of origami folding further expands its applicability in metamaterial development; one pattern can be scaled up to architecture size^[31,32] or scaled down to a nanometric level^[33,34] without altering the basic folding-induced properties.

In this paper, we propose and demonstrate a new mechanism to achieve programmability in origami-based metamaterials. Here, rather than relying on structural multistability, a self-locking-based strengthening mechanism is employed to tune the kinematical and mechanical properties. Note that, the current state of the art of origami engineering mainly centralizes on flat-foldable origamis because they could significantly reduce the size and volume of the structure and therefore, facilitate packaging and transportation; however, flat-foldable

Dr. H. Fang, S.-C. A. Chu, Y. Xia, Prof. K. W. Wang
Department of Mechanical Engineering
University of Michigan
Ann Arbor 48105, USA
E-mail: hongbinf@umich.edu

 The ORCID identification number(s) for the author(s) of this article can be found under <https://doi.org/10.1002/adma.201706311>.

DOI: 10.1002/adma.201706311

origamis account for a very small portion of the origami library. For example, in the simplest degree-4 vertex origami family, flat-foldable patterns (including the well-studied Miura-ori^[35,36]) only cover very limited design space; the majority of 4-vertex origamis are nonflat-foldable.^[37,38] Instead of being folded flat, they will “self-lock” at a nonflat configuration prescribed by the crease pattern.^[38] Hence, it is interesting to explore whether the broader design library of nonflat-foldable origamis would provide new bases for creating reconfigurable metamaterials, and whether the additional “locking” would become a new tool other than multistability to program mechanical properties. Nevertheless, the research on exploiting the mechanical properties of nonflat-foldable origamis is still largely nonexistent.

To advance the state of the art, in this research we focus on a representative nonflat-foldable degree-4 vertex origami, the single-collinear (SC) pattern, and combine experiments with finite element analyses alongside analytical models to explore a reconfigurable origami metamaterial, whose stiffness can be discretely programmed and tuned through the locking of constituent cells. Under the ideal rigid-foldable assumption, the SC origami would self-lock at prescribed configuration, therefore offering extra design freedom beyond the traditional Miura-ori to program the metamaterial's foldability and relative density. While for a practical nonrigid SC origami, its deformation involves two qualitatively different modes: the prelocking folding and the postlocking pressing. The fundamental difference between the two modes lies in the origin of the stiffness. In the folding mode, the origami exhibits relatively low stiffness that comes from the bending of the crease; while in the pressing mode, the origami will have much higher stiffness that is attributed to the bending or twisting of the origami facets. Hence, when switching between the two modes, the structural stiffness experiences a significant jump, giving rise to a two-segment piecewise profile. The stiffness-jump property is generalized by connecting multiple SC cells in series into a metamaterial, whose stiffness can take different values corresponding to different locking configurations. We show that the stiffness can be reversibly programmed via either passive or active switching of the constituent cells' deformation modes. Finally, we demonstrate that the locking-induced piecewise stiffness additionally endows the metamaterials with unique dynamic characteristics, highlighting its broad range of potential applications in morphing and vibration control.

The concept of self-locking origami mechanical metamaterials is shown in **Figure 1a–c**, where the basic constituent element is a degree-4 vertex origami cell with a single pair of collinear creases (i.e., an SC cell). In rigid origami, the cell is composed of four inflexible zero-thickness parallelograms that are connected by four creases. The vertex is the point where four creases intersect. The geometry of an SC cell can be characterized by two collinear crease lengths a_1, a_2 , two zig-zag crease lengths b_1, b_2 , and two sector angles γ_1, γ_2 (**Figure 1a**). Without loss of generality, we assume $0 < \gamma_1 < \pi/2$ and $\gamma_1 < \gamma_2 < \pi - \gamma_1$. Rigid folding of an SC cell is a one degree-of-freedom (DoF) motion, which will stop at a nonflat configuration due to the binding of facets “I” and “II” (since $\gamma_1 < \gamma_2$).^[39] Such a phenomenon is named as “self-locking.” As the constituent element, the SC cell can be periodically repeated in two directions into a 2D sheet (**Figure 1b**). Moreover, two SC cells satisfying

compatibility constraints (Section IA, Supporting Information) can be stacked into a 3D cell (in nested-in or bulged-out configurations), which can be further tessellated in three directions into a 3D block (**Figure 1c**). If assuming ideal kinematic constraints at the connections between two SC cells or two 3D cells, the 2D sheets and 3D blocks remain a single DoF for folding and preserve self-locking capability; their folding kinematics and self-locking behaviors are completely determined by the constituent SC cells.

The kinematics of a rigid SC cell depends on both the crease lengths and the sector angles. Here, we focus on two important kinematic quantities: one is the SC cell or the 3D cell's foldability (η) defined as the ratio between the maximum foldable length (ΔL_{\max}) and the maximum length (L_0), i.e., $\eta = \Delta L_{\max} / L_0$, where $\Delta L_{\max} = L_{\max} - L_{\text{SL}}$, and L_{SL} is the length at the self-locking configuration; the other is the 3D cell's relative density (ρ) defined as the ratio between the mass of all facets (m) and the enclosed volume (V), i.e., $\rho = m/V$ (Section IA, Supporting Information). As an example, we study a 3D cell (in bulged-out configuration) composed of two identical SC cells, with $b_2/b_1 = 1$. **Figure 1d,e** illustrates the effects of the sector angles γ_1 and γ_2 on the deformability η and the reciprocal of the normalized density at the self-locking configuration ($1/\hat{\rho}_{\text{SL}}$) (see other cases with $b_2/b_1 = 2$ and $b_2/b_1 = 0.5$ in **Figures S3** and **S4**, Supporting information). It reveals that the SC pattern possesses much wider design space than the traditional Miura-ori for metamaterial development, where the latter only occupies the diagonal $\gamma_1 = \gamma_2$, a degenerate case of the SC design. **Figure 1d,e** also reveals a large range of achievable η and $\hat{\rho}_{\text{SL}}$; while on the contrary, η and $\hat{\rho}_{\text{SL}}$ are not programmable for the Miura-ori designs. Therefore, by tailoring the design parameters (a_1, a_2, b_1, b_2 , and γ_1, γ_2), one has a large space to regulate the metamaterials' foldability and relative density.

We remark here, that in addition to the above homogeneous tessellation based on a single type of SC cell, self-locking origami metamaterials can also be heterogeneously constructed based on multiple different flat-foldable Miura-ori cells. With geometry constraints, two Miura-ori cells can be connected together and remain a single DoF for folding. At the connection between two Miura-ori cells, a new SC cell is generated, which prevents the overall hybrid origami from folding flat, i.e., the hybrid origami receives extra self-locking ability. More details on the kinematics and advantages of heterogeneously constructed self-locking origami can be found in Section IB, Supporting Information.

Proof-of-concept self-locking origami prototypes can be fabricated with different materials via different methods. As examples, we fabricate four prototypes of the 3D-stacked SC cell (in nested-in configuration), namely, an assembled steel prototype, a 3D-printed flexible photoreactive resin (FPR) prototype, a 3D-printed elasto plastic (EP) prototype, and a silicone elastomer prototype (based on soft lithography technique) (**Figure 2a**, detailed prototyping materials and procedures can be found in Section IIA, Supporting Information). In the steel prototype, the facets and creases are very thin, and the steel facets are much stiffer than the polyethylene creases so that rigid folding can be well ensured before self-locking. In the 3D-printed prototypes and the silicone elastomer prototype, the facets are designed to be 5 mm in thickness, and the

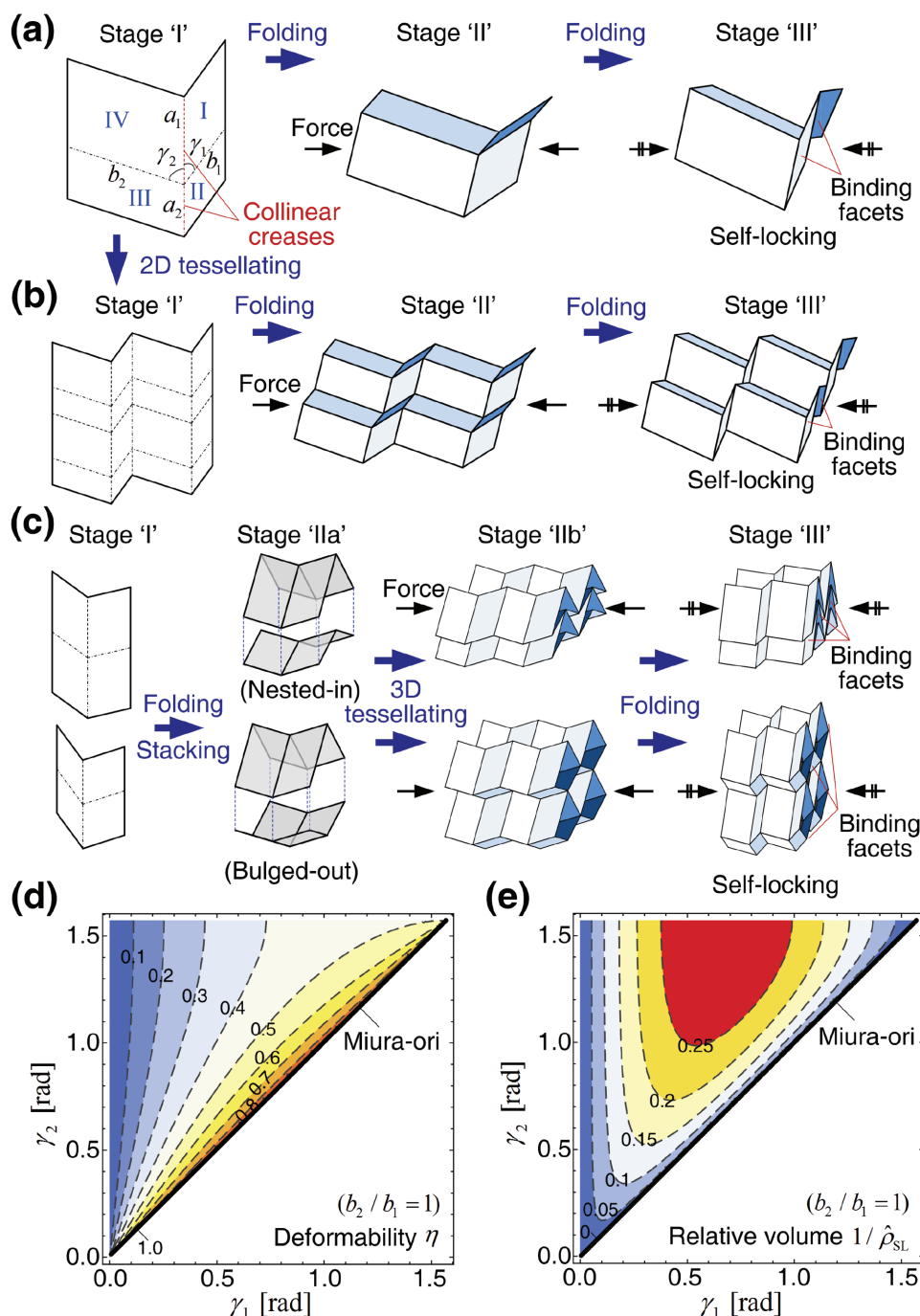


Figure 1. Kinematics of self-locking origami mechanical metamaterials. a) Geometry and self-locking of an SC cell, where the collinear creases are denoted. It can be homogeneously constructed into: b) a 2D SC sheet and c) 3D SC blocks (nested-in and bulged-out configurations), which inherit the self-locking capability. By applying external forces, the SC origami cell, sheet, and blocks can fold effectively from a flat state (stage “I”) to a partially folded state (stage “II”) and finally self-lock at stage “III” because two or more facets bind together. The arrow with double strokes indicates the limiting of further deformation in that direction. With SC designs, a large range of: d) the deformability η and e) the normalized relative volume $1/\hat{\rho}_{SL}$ (i.e., the reciprocal of the normalized density) at the self-locking configuration can be achieved by programming the sector angles γ_1 and γ_2 ; here, the 3D cell (in bulged-out configuration) is stacked by two identical SC cells, and $b_2/b_1 = 1$. In (d) and (e), the symmetric part corresponding to $\pi/2 < \gamma_2 < \pi$ is omitted.

creases are much thinner than the facets (e.g., 1, 2, or 3 mm) to facilitate folding. To prevent stress concentration, the transitions between facets and creases are smoothed, and the vertices are perforated. Note that in practice, using one material to

prototype based on 3D-printing or soft lithography techniques is desirable. However, in these prototypes, the crease and facet thicknesses cannot be ignored, and the stiffness difference between facets and creases may not be significant enough such

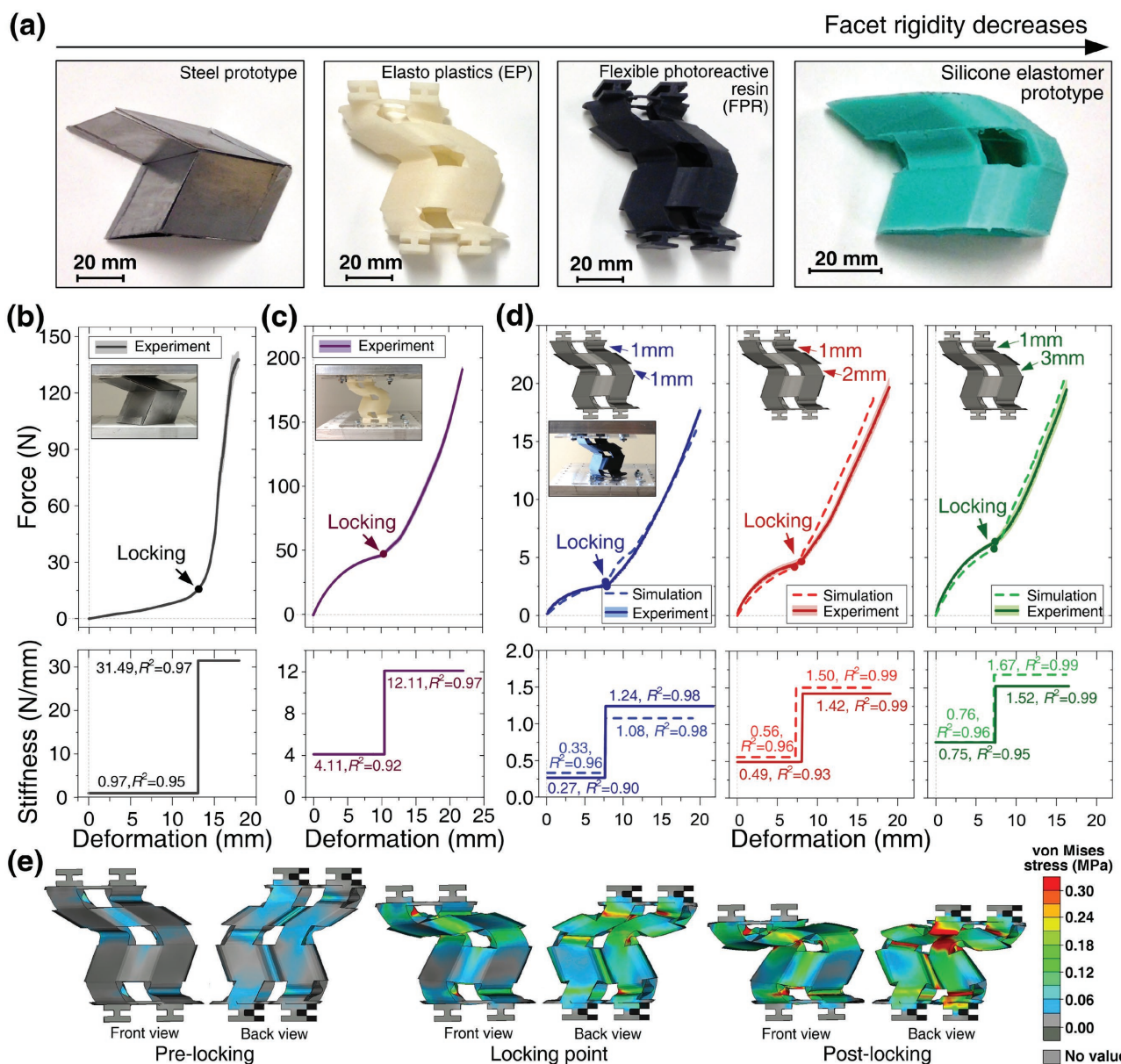


Figure 2. Prototypes of 3D SC cells and their mechanical responses under compressions. a) From left to right showing the steel prototype, the 3D-printed EP prototype, FPR prototype, and the silicone elastomer prototype. The force–deformation curves (top) and the linearly fitted stiffness (bottom) of: b) the steel prototype, c) the EP prototype (with collinear-crease thickness 1 mm), and d) the FPR prototypes (with collinear-crease thickness 1, 2, and 3 mm, respectively) are given, where the solid curves and the shaded bands denote the averages and standard deviations of four tests, respectively. The coefficient of determination (R^2) is given for each case. e) The von Mises stress distribution of an EP model obtained from FE analyses, where the collinear creases are 2 mm in thickness.

that zero-thickness and rigid-folding kinematics cannot be fully assumed.

Note that under compression, an ideal rigid origami cannot be compressed after reaching the self-locking point. However, practically, the prototypes' materials have flexibility such that they can be further deformed after locking. Hence, in addition to kinematics, we also investigate the mechanical property changes induced by self-locking through experiments and FE analysis, with the 3D cells as examples in the follow-up studies. We first perform displacement-controlled compression tests on the steel prototype, the EP prototype, and the FPR

prototypes; the obtained force–deformation curves are displayed in Figure 2b–d, respectively. A common characteristic is revealed in these tests that when passing through the self-locking point, the force–deformation curves show significant changes of slopes. Linear regression analyses indicate that such slope increases correspond to the jumps of equivalent stiffness. If defining λ as the ratio between the postlocking stiffness and the prelocking stiffness, we have $\lambda_{\text{steel}} = 32.5$ for the steel prototype, $\lambda_{\text{EP}} = 2.9$ for the EP prototype, and $\lambda_{\text{FPR}_1\text{mm}} = 4.6$, $\lambda_{\text{FPR}_2\text{mm}} = 2.9$, $\lambda_{\text{FPR}_3\text{mm}} = 2.0$ for the FPR prototypes with collinear-crease thickness 1, 2, and 3 mm,

respectively. The essence of these stiffness jumps lies in the different origins of stiffness in the prelocking and postlocking deformation modes. In the prelocking mode, the cell's deformation mainly comes from folding, and the stiffness mainly originates from the bending stiffness of the creases. While in postlocking mode, folding is largely prohibited by the binding of certain facets; in addition to crease bending, the origami facets will also be bent or twisted, giving rise to a noticeable increase of stiffness. This is evident from the FE analysis on the FPR model, where under displacement-controlled compression the stress distribution gradually extends from the creases to the facets and becomes significant after self-locking (Figure 2e). Hence after self-locking, further compressive deformation will be constrained by the relatively higher stiffness, providing that the deformation does not exceed the limit for mechanical or material failure.

Experiments also indicate that the prelocking and postlocking stiffness values depend on the crease and facet materials been used. For example, the prelocking stiffness of the steel prototype is relatively low because of the flexible creases made of polyethylene films and prebent spring-steel stripes; whereas the postlocking stiffness receives a more than 30 times increase that results from the rigid steel facets. For another example, the prelocking and postlocking stiffness of the EP prototype are much higher than those of the FPR prototype (with the same geometry) because the elasto plastics is much more rigid than the flexible photoreactive resin (see material characterization in Section IIB, Supporting Information). Moreover, the relationship between the stiffness values and the crease thickness is revealed through experiments and numerical analysis. Figure 2d illustrates that by increasing the thickness of the collinear creases of the 3D cells, both the prelocking and postlocking stiffness of the FRP prototype enjoys certain growth; while the corresponding stiffness jump ratio decreases instead because the facet thickness is constant and the locking-induced stiffness-increases remain largely unchanged. These findings enable us to effectively program the prelocking and postlocking stiffness via tuning the geometries and materials of the creases or facets. Details on the experiments and FE analyses can be found in Sections IIC and IIIA, Supporting Information.

With the locking-induced stiffness jump in a single 3D cell, a reasonable hypothesis is that if several self-locking cells with the same geometry but different stiffness profiles are connected in series, a piecewise stiffness with multiple stiffness segments can be achieved because of multiple asynchronous self-locking. Here, we remark that if the cells are connected under ideal kinematic constraints, all cells will fold following kinematics and will self-lock simultaneously, giving rise to only one stiffness jump. However, in a nonideal scenario where weak kinematic constraint, or particularly, no kinematic constraint is applied to the connections, the constituent cells are no longer kinematically related. Their folding and locking are independent and could be asynchronous, and multiple-segment piecewise stiffness can thus be achieved; this is manifested by experiments and FE analyses. In the experiment, we connect three layers of FPR prototypes in series (namely, layer #1, #2, and #3 from top to bottom); each layer consists of two cells with the same geometry (see the inset of Figure 3a; the collinear-crease thickness of the cells in layers #1, #2, and #3 is 1, 2, and 3, respectively,

and all the other creases are of the same thickness, 1 mm), and they are assembled with rigid plates in opposite orientations to ensure stability. The plates in neighboring layers are rigidly connected, while the prototypes in neighboring layers are not kinematically constrained so that their folding and locking are independent to each other. Hence, when being compressed, deformation of the three-layer prototype is no longer 1-DoF; rather, due to force balance among layers, the cells in layer #1 first self-lock and enter the pressing mode due to their relatively low prelocking stiffness, and then the cells in layer #2 and layer #3 self-lock successively (Figure 3c). Figure 3a reports the experimental and FE force–deformation curves during a displacement-controlled compression test. By identifying the locking points in experiments and numerical analyses, the force–deformation curve is divided into four segments (i.e., no lock, layer #1 locks, layers #1, 2 lock, and layers #1, 2, 3 lock) with different slopes, which correspond to four stiffness segments with gradually increasing values.

In addition to the piecewise stiffness obtained in the above passive compression process, the three-layer metamaterial could exhibit other stiffness values if the locking configuration of each constituent cell can be actively controlled. To show this potential, in FE analyses we first lock the cells in layer #2, layer #3, or layers #2 and #3 by applying a compressive force so that the corresponding cells stay in the pressing mode, and then proceed to compress the model through displacement control. Figure 3b shows the force–deformation curves and the linearly fitted stiffness, where new locking configurations that cannot be achieved in the passive compression process are observed, such as layer #2 locks prior to layers #1 and #3. These new configurations thus correspond to new stiffness values. Details on the multilayer experiments and FE analyses can be found in Sections IIC and IIIB, Supporting Information.

To better understand the nature of the programmable stiffness observed in our experiments and FE analyses, an equivalent spring model is developed (Figure 3d). A single self-locking cell can be modeled by two linear springs connected with a rigid plate. The two springs are of different lengths and different stiffness. Their length difference represents the foldable length determined by the origami geometry; the longer spring stiffness k_1 denotes the prelocking stiffness originates from crease bending, whereas the shorter spring stiffness k_2 indicates the stiffness increase coming from the bending or twisting of the facets (generally, $k_1 \ll k_2$). Hence at the beginning stage of compression, the longer spring is compressed, corresponding to the prelocking folding mode with stiffness k_1 ; then the shorter spring will be contacted, and after that both springs take effect, corresponding to the postlocking pressing mode with an increased stiffness $k_1 + k_2$. Such a single-cell model can be connected in series, e.g., Figure 3d also shows an n -layer model, where the constituent layers are identical in geometry but different in spring stiffness values (for layer i , the longer and shorter spring stiffness are k_{i1} and k_{i2} , respectively, $i = 1, 2, \dots, n$). Theoretically, based on whether each constituent cell stays in the folding mode or the pressing mode, the n -layer model possesses 2^n different locking configurations, corresponding to 2^n stiffness values providing that the constituent cells' stiffness profiles are prior obtained (see Section IVA, Supporting Information). Furthermore, these target stiffness

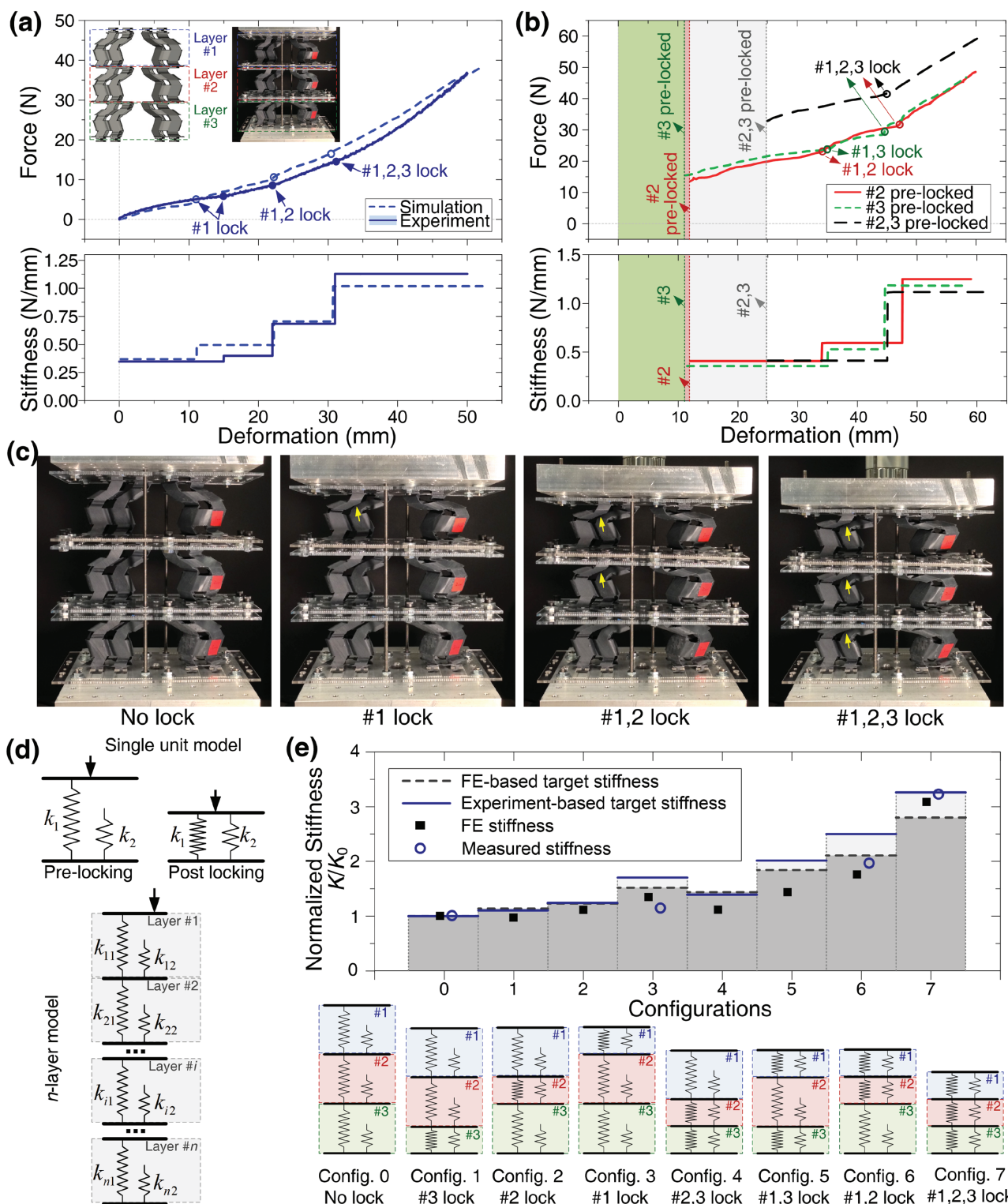


Figure 3. Experiments, FE analyses, and equivalent models of the multilayer self-locking metamaterial. a) In a passive compression process, experiments and FE analyses reveal a four-segment piecewise stiffness profile, where the solid curves and the shaded bands denote the averages and standard deviations of four tests, respectively. b) By actively locking certain cells prior, new locking configuration and new stiffness values can be achieved during compressing. c) Photos of the three-layer metamaterial under displacement-controlled compression, where the locking points are indicated by arrows. d) The equivalent spring models. e) Stiffness values obtained from experiments (circles) and FE analyses (squares) corresponding to the eight different configurations. Solid and dashed lines denote the experiment-based and FE-based target stiffness, respectively. All the stiffness values are normalized with respect to the stiffness at the nonlocking configuration "0."

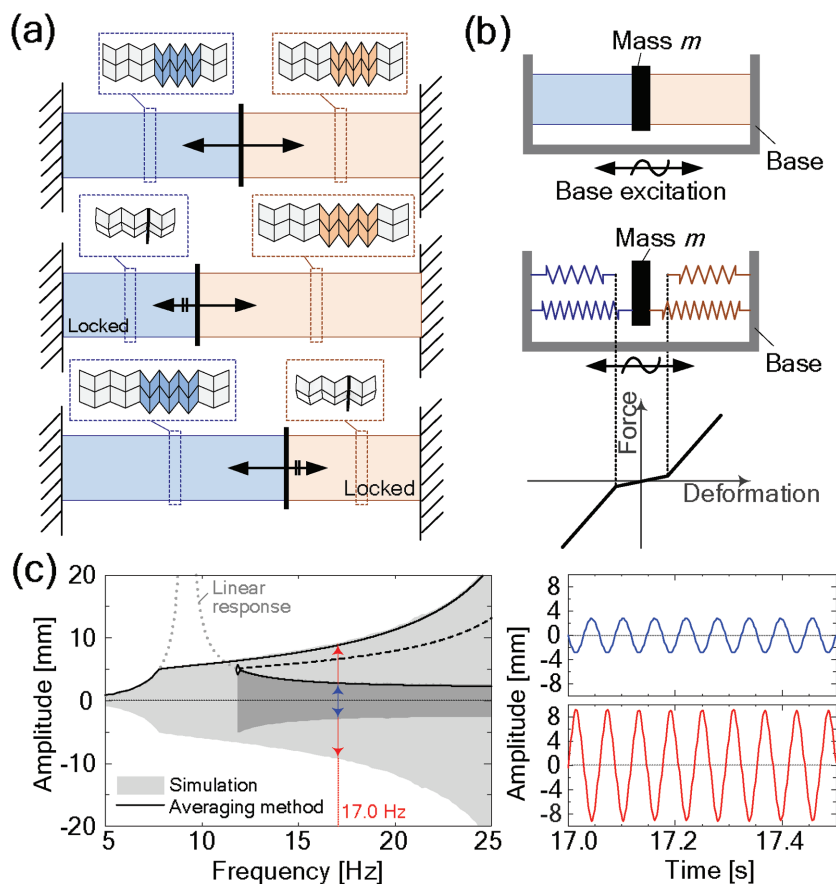


Figure 4. Static limiting-stopper effect and its dynamic characteristics. a) A schematic illustration of the self-locking origami metamaterial with bidirectional limiting-stopper effect; insets show the configurations of heterogeneously constructed self-locking origamis. The arrow with double strokes indicates the limiting of further deformation in that direction. b) Schematic illustrations of a bidirectional limiting-stopper under base excitations and its equivalent dynamic model. c) The relative amplitude–frequency response (left) and characteristic time-histories (right) of the lumped mass under harmonic base excitations. The base excitation amplitude is 2 mm. The right-top and right-bottom show the low-amplitude and high-amplitude time histories of the relative displacement at excitation frequency 17.0 Hz.

is achievable and on-line controllable by strategically switching the modes of the constituent cells through passive or active means. As an example, Figure 3e displays the eight locking configurations of the three-layer prototype and the corresponding target stiffness, as well as the stiffness resulting from experiments and FE analysis. This excellent in situ stiffness tuning capability well illustrates the power of self-locking.

Our combined experimental and numerical results indicate that by exploiting the self-locking origami in design, the metamaterial would be equipped with limiting-stopper functionality. That is, within the permitted range, the compressive deformation can be easily achieved by folding because of the low prelocking stiffness; while beyond the range, further deformation will be limited by high postlocking stiffness. Such limiting-stopper effect is desirable in shape morphing applications, where the shape changing process need to be realized via low actuation, while the target configuration (i.e., the locked configuration) calls for high carrying capacity and the ability to limit excessive deformations. Moreover, the abovementioned

excellent programmability of self-locking origami offers the limiting-stopper with strong tunability. The permissible deformation can be tailored via altering the geometry design of SC cells, or more preferably, through adjusting the composition of Miura-ori cells in a heterogeneous construction; and the effect of the stopper can be controlled by tuning the prelocking and postlocking stiffness through crease and facet material selection. In addition to constraining compressive deformations, the limiting-stopper functionality can also be extended to bidirectional via connecting two precompressed origami components (Figure 4a). The bidirectional limiting can be symmetric or asymmetric in terms of the permissible range and the stopping effect.

While the above reported results all fall in the static realm, the locking-induced piecewise stiffness can further trigger extraordinary dynamics when subjected to periodic excitations. For example, Figure 4b shows a lumped mass that is connected to the base via a self-locking metamaterial with bidirectional limiting-stopper functionality; the base is subjected to harmonic base excitation. The system can be equivalently described by a single DoF lumped mass model with piecewise stiffness profile. Figure 4c shows the relative amplitude–frequency responses of the system (details on the dynamic analyses can be found in Section V, Supporting Information). Results from numerical analyses are denoted by gray shadow, with the light and dark gray representing the coexisting responses with high and low amplitudes at the same excitation frequency, respectively. The responses are also predictable by using the method

of averaging (solid curves), where the unstable solutions and bifurcation point are represented by dashed lines and diamond marker, respectively. Both numerical and approximation analyses clearly illustrate a dynamically bistable region where both high-amplitude and low-amplitude responses are possible. Comparing with the corresponding linear system (dotted curve), the self-locking metamaterial exhibits a much wider band of high-amplitude responses, which can be utilized for broadening the effective bandwidth of vibration absorption^[40] or energy harvesting.^[41] On the other hand, in the linear resonance zone, surprisingly, the amplitude is significantly depressed, which has the potential to be exploited for vibration isolation.^[42]

It is worth noting that other origami locking mechanisms have also been proposed, which can be categorized into two major types. In the first types, locking is achieved by contacting or assembling of additional mechanical locking elements, including alignment features and locking latches,^[43] as well as angle lock layers.^[44] In the other type, active-material-based

locking mechanisms, such as surface-tension-driven liquid locking hinges^[19,45,46] and shape memory composites,^[47] are employed for fixing the structure at a specific configuration. Our approach shows fundamental differences and advantages over the prior art, mainly in two aspects. First, previous locking mechanisms only aimed at fixing the origami structure at specified configurations during folding; our approach can meanwhile significantly alter the mechanical stiffness and dynamical responses. Second, the presented facet-binding based locking mechanism neither calls for additional mechanical locking elements nor needs active materials, which simplifies the design and improves the overall robustness.

In conclusion, we have combined experiments and numerical analyses to demonstrate that the nonflat-foldable origamis provide a new platform for the design of metamaterials with programmable kinematic and mechanical properties. The programmability originates from the locking and reconfiguration of the nonflat-foldable origami. Specifically, we have shown that the SC cell, a typical self-locking origami, could significantly expand the geometry design space so that the corresponding metamaterial's foldability and relative density can be programmed in a wide range. Moreover, under compression the SC origami exhibits a jump of stiffness because of the switch of deformation modes, yielding a piecewise linear stiffness profile. This is verified by our proof-of-concept prototypes made of different materials via different methods and FE analysis. Importantly, the constituent self-locking cells with the same crease pattern but different piecewise stiffness profiles can be connected in series with no kinematic constraint so that locking of the cells will happen asynchronously under compression, generating a multisegment piecewise stiffness. The stiffness can also be on-line controlled via strategically locking the constituent cells if active folding mechanism is embedded. The self-locking origami metamaterial proposed here presents two main differences with respect to the existing origami metamaterials: first, unlike the rigid-foldable origami, here both the origami geometry and the composition materials play roles in achieving the target stiffness; second, the stiffness programmability does not originate from structural multistability but from a strengthening mechanism induced by self-locking. Additionally, while the current origami research mainly locates in the kinematics and statics realms, this research demonstrates that the locking-induced piecewise stiffness could also trigger non-conventional dynamics under harmonic excitations, including a low-amplitude response at the linear-resonance zone and broad bandwidth of high-amplitude responses. Last but not least, while here the studies are based on prototypes at centimeter scale made of limited types of material, the proposed design can be extended to different material and scales. For example, by using photolithography for patterning and electro-deposition for fabrication, the facets and creases can be scaled down to 15 and 1.5 μm , respectively;^[45] the high precision of e-lithography can further reduce the origami size to nanometer level.^[34] As such, our study provides new opportunities for designing mechanical metamaterials and metastructures capable of achieving customizable kinematical, mechanical, and dynamical properties that can be of particular interest for potential applications in morphing, vibration control, and energy harvesting.

Supporting Information

Supporting Information is available from the Wiley Online Library or from the author.

Acknowledgements

The authors would like to thank Dr. Suyi Li for the inspiring discussions that were of great benefit to this work. This research was partially supported by the National Science Foundation under award No. 1634545, the University of Michigan Collegiate Professorship, and the University of Michigan Summer Undergraduate Research in Engineering (SURE) program.

Note: The presentation of the author name Kon-Well Wang was corrected after initial publication online.

Conflict of Interest

The authors declare no conflict of interest.

Keywords

degree-4 vertex origami, mechanical metamaterials, metastructures, origami dynamics, piecewise stiffness

Received: October 31, 2017

Revised: November 29, 2017

Published online: March 7, 2018

- [1] G. W. Milton, A. V. Cherkaev, *J. Eng. Mater. Technol.* **1995**, 117, 483.
- [2] M. Kadic, T. Bückmann, N. Stenger, M. Thiel, M. Wegener, *Appl. Phys. Lett.* **2012**, 100, 191901.
- [3] H. M. A. Kolken, A. A. Zadpoor, *RSC Adv.* **2017**, 7, 5111.
- [4] X. Hou, V. V. Silberschmidt, in *Mechanics of Advanced Materials: Analysis of Properties and Performance*, (Eds: V. V. Silberschmidt, V. P. Matveenko), Springer, Cham, Switzerland **2015**, pp. 155–179.
- [5] A. A. Zadpoor, *Mater. Horiz.* **2016**, 3, 371.
- [6] C. Coulais, J. T. B. Overvelde, L. A. Lubbers, K. Bertoldi, M. Van Hecke, *Phys. Rev. Lett.* **2015**, 115, 1.
- [7] A. Rafsanjani, A. Akbarzadeh, D. Pasini, *Adv. Mater.* **2015**, 27, 5931.
- [8] S. Shan, S. H. Kang, J. R. Raney, P. Wang, L. Fang, F. Candido, J. A. Lewis, K. Bertoldi, *Adv. Mater.* **2015**, 27, 4296.
- [9] R. L. Harne, K. W. Wang, *Smart Mater. Struct.* **2013**, 22, 23001.
- [10] R. L. Harne, K. W. Wang, *Harnessing Bistable Structural Dynamics: For Vibration Control, Energy Harvesting, and Sensing*, John Wiley and Sons, Chichester, UK **2017**.
- [11] B. Florijn, C. Coulais, M. van Hecke, *Phys. Rev. Lett.* **2014**, 113, 175503.
- [12] J. Shim, S. Shan, A. Košmrlj, S. H. Kang, E. R. Chen, J. C. Weaver, K. Bertoldi, *Soft Matter* **2013**, 9, 8198.
- [13] A. Rafsanjani, D. Pasini, *Extreme Mech. Lett.* **2016**, 9, 291.
- [14] R. L. Harne, Z. Wu, K. W. Wang, *J. Mech. Des.* **2015**, 138, 21402.
- [15] Z. Wu, Y. Zheng, K. W. Wang, *arXiv Prepr.* **2017**, arXiv:1709.01800.
- [16] Y. Shan, M. Philen, A. Lotfi, S. Li, C. E. Bakis, C. D. Rahn, K. W. Wang, *J. Intell. Mater. Syst. Struct.* **2008**, 20, 443.
- [17] N. Kidambi, R. L. Harne, K. W. Wang, *Smart Mater. Struct.* **2017**, 26.
- [18] A. Lebé, *Int. J. Space Struct.* **2015**, 30, 55.
- [19] C. L. Randall, E. Gultepe, D. H. Gracias, *Trends Biotechnol.* **2012**, 30, 138.
- [20] S. Felton, M. Tolley, E. Demaine, D. Rus, R. Wood, *Science* **2014**, 345, 644.

- [21] P. M. Reis, F. López Jiménez, J. Marthelot, *Proc. Natl. Acad. Sci. USA* **2015**, *112*, 201516974.
- [22] M. Thota, S. Li, K. W. Wang, *Phys. Rev. B* **2017**, *95*, 64307.
- [23] S. Li, H. Fang, K. W. Wang, *Phys. Rev. Lett.* **2016**, *117*, 114301.
- [24] L. H. Dudte, E. Vouga, T. Tachi, L. Mahadevan, *Nat. Mater.* **2016**, *15*, 583.
- [25] J. T. B. Overvelde, J. C. Weaver, C. Hoberman, K. Bertoldi, *Nature* **2017**, *541*, 347.
- [26] J. L. Silverberg, A. A. Evans, L. McLeod, R. C. Hayward, T. Hull, C. D. Santangelo, I. Cohen, *Science* **2014**, *345*, 647.
- [27] S. Li, K. W. Wang, *J. R. Soc., Interface* **2015**, *12*, 20150639.
- [28] S. Waitukaitis, R. Menaut, B. G. Chen, M. van Hecke, *Phys. Rev. Lett.* **2015**, *114*, 55503.
- [29] H. Fang, K. W. Wang, S. Li, *Extreme Mech. Lett.* **2017**, *17*, 7.
- [30] H. Fang, S. Li, H. Ji, K. W. Wang, *Phys. Rev. E* **2017**, *95*, 52211.
- [31] E. T. Filipov, T. Tachi, G. H. Paulino, *Proc. Natl. Acad. Sci. USA* **2015**, *112*, 12321.
- [32] M. Thota, K. W. Wang, *J. Appl. Phys.* **2017**, *122*, 154901.
- [33] Z. Song, C. Lv, M. Liang, V. Sanphuang, K. Wu, B. Chen, Z. Zhao, J. Bai, X. Wang, J. L. Volakis, L. Wang, X. He, Y. Yao, S. Tongay, H. Jiang, *Small* **2016**, *12*, 5401.
- [34] V. B. Shenoy, D. H. Gracias, *MRS Bull.* **2012**, *37*, 847.
- [35] M. Schenk, S. D. Guest, *Proc. Natl. Acad. Sci. USA* **2013**, *110*, 3276.
- [36] S. Li, K. W. Wang, *Smart Mater. Struct.* **2015**, *24*, 105031.
- [37] S. Waitukaitis, M. van Hecke, *Phys. Rev. E* **2016**, *93*, 23003.
- [38] H. Fang, S. Li, H. Ji, K. W. Wang, *Phys. Rev. E* **2016**, *94*, 43002.
- [39] H. Fang, S. Li, K. W. Wang, *Proc. R. Soc. London, Ser. A* **2016**, *472*, 20160682.
- [40] X. Shui, S. Wang, *Mech. Syst. Signal Process.* **2018**, *100*, 330.
- [41] H. Liu, C. Lee, T. Kobayashi, C. J. Tay, C. Quan, *Smart Mater. Struct.* **2012**, *21*, 35005.
- [42] D. M. Running, J. B. Ligon, I. Miskioglu, *J. Vib. Control* **2004**, *10*, 1775.
- [43] N. S. Shaar, G. Barbastathis, C. Livermore, *J. Microelectromech. Syst.* **2015**, *24*, 1043.
- [44] D. Deng, Y. Chen, *J. Mech. Des.* **2014**, *137*, 21701.
- [45] T. G. Leong, P. A. Lester, T. L. Koh, E. K. Call, D. H. Gracias, *Langmuir* **2007**, *23*, 8747.
- [46] S. Pandey, M. Ewing, A. Kunas, N. Nguyen, D. H. Gracias, G. Menon, *Proc. Natl. Acad. Sci. USA* **2011**, *108*, 19885.
- [47] S. M. Felton, M. T. Tolley, B. Shin, C. D. Onal, E. D. Demaine, D. Rus, R. J. Wood, *Soft Matter* **2013**, *9*, 7688.